Erosion mechanism of refractories in a pyro-processing furnace for recycling lithium-ion secondary batteries

Yoshiki Murakami[a,b], Yutaka Matsuzaki[b], Takeshi Kamimura[b], Takato Nishiura[b], Koichi Masuda[b], Atsushi Shibayama[a], Ryo Inoue[a,*]

[a] Graduate School of International Resource Sciences, Akita University, 1-1, Tegatagakuen-machi, Akita, 010-8502, Japan
[b] Technical Division, Nakajima Plant, Nippon Recycle Center Corp., Osaka, 555-0041, Japan

A B S T R A C T

The refractory lining in a furnace is always damaged and peels off when spent lithium-ion secondary batteries (LIB) are pyro-processed in a rotary kiln. To develop highly durable refractories and to elucidate the erosion behavior, various analyses such as scanning electron microscopy/energy dispersive X-ray spectroscopy, laser-induced breakdown spectroscopy, inductively coupled plasma atomic emission spectroscopy, ion chromatography, and X-ray diffraction were performed on the linings sampled from different sections of a refractory. Our results suggested the following mechanisms in Al_2O_3–SiO_2–CaO refractory damage during pyro-processing of spent LIB packs. First, Li_2O, P_2O_5, LiF, and HF were formed by thermal decomposition of electrolyte constituents of the lithium-ion secondary batteries. When HF reacts with SiO_2, Al_2O_3, and CaO on the surface of the refractory, each fluoride that forms vaporizes and melts. When Li_2O and P_2O_5 (as well as LiF) react with the Al_2O_3–SiO_2 refractory, an Li_2O–Al_2O_3–SiO_2–P_2O_5(-LiF) phase with a low melting point forms and penetrates into the refractory through pores, grain boundaries, and cracks, resulting in peeling off.

1. Introduction

With the proliferation of mobile devices, such as notebook personal computers, smartphones, and hybrid and electric cars, the demand for secondary batteries as power sources has rapidly increased. Among these secondary batteries, the ratio of lithium-ion batteries (LIBs) has markedly increased. Compared with nickel–cadmium and nickel–hydrogen batteries, LIBs have the advantage of a higher energy density, longer life cycle, and lighter weight, resulting in increased demand. According to a report by a survey institution, by 2020, the global market size for LIBs is predicted to be 1.5 times that of 2015 [1].

In an LIB positive electrode, active ingredients such as $LiCoO_2$, $LiNiO_2$, $LiMn_2O_4$, $Li(Co,Ni)O_2$, and $Li(Co,Ni,Mn)O_2$, are applied on an electric (current) collector Al foil. In an LIB negative electrode, active ingredients, such as graphite, are applied on an electric collector Cu foil. Recently, carbon-rich Si-containing ceramics [2] and Si–$FeSi_2$/C nanocomposite materials [3] have been developed as anode candidates, but pure graphite is still mainstream. The electrolyte consists of lithium salts, such as $LiPF_6$ and $LiBF_4$, dissolved in an organic solvent, such as ethylene carbonate and diethyl carbonate. For the outer case, steel cans, aluminum cases, and aluminum laminate are used. Considering the

increase in demand for LIBs and the constituents of LIBs, from the standpoint of recycling resources and securing materials, recycling of expensive materials in spent LIBs, such as lithium, cobalt, and nickel, is desired. Additionally, efforts to make batteries lighter with higher performance have increased the need for a larger amount of highly expensive rare metals, resulting in increased demand for low-cost recycled materials. Under such circumstances, although studies on LIB recycling technology are being actively pursued [4–9], most involve single-element recovery through various wet chemical processes.

To facilitate LIB recycling, it is effective to first disassemble the LIB pack, but there is a risk of ignition from the reaction between the electricity remaining in the LIB and the organic solvent during disassembly. Therefore, in mass LIB recycling processes, spent LIB packs are first heat-treated without disassembling to remove the organic solvent, and mechanical separation (grinding, sieve sorting, magnetic sorting, etc.) is carried out [4–8]. In these studies, although pyro-processing is a simple operation, the necessity of installing devices to purify the smoke and gas generated from the combustion of carbon and organic compounds has been reported. Therefore, such processes are expected to have the drawback of infeasibility of recovery of organic compounds. A recent study has reported the viability of

---

commercializing recycling technology for LIBs used in cars [10].

As a small-scale recycling business involving lithium-ion secondary batteries, pyro-processing in a rotary kiln is used for the removal of organic matter, such as the organic compounds present in LIBs and the separator [11]. After this pyro-processing, using mechanical separation and the residual valuable solids, the resources can be recycled. Regarding pyro-processing of spent LIBs in a rotary kiln, although the recovery rate of each element in the valuable solid material has been described [12], the refractory lining inside the kiln, which consists of mullite with dispersed coarse Al_2O_3 particles, is eroded and damaged. A study on the corrosion of mullite and SiC refractories by cathode materials has been reported [13], but the erosion mechanism of the refractories by Li_2O, P_2O_5, and HF, which are generated by the thermal decomposition of the electrolyte contained in the spent LIB packs, has not been determined.

As a part of the research to develop highly durable refractories and to improve the refractory life, the erosion damage mechanism of refractory material in a rotary kiln during pyro-processing of LIB packs with an $LiCoO_2$ positive electrode was examined in this study.

2. Experimental procedure and analysis

2.1. Sampling of refractory material

Fig. 1 shows the schematic of the business facilities where pyro-processing of LIB packs is performed in a rotary kiln (outer diameter: 1.6 m, inner diameter: 1.0 m, length: 5.0 m) to recycle small-scale spent lithium-ion secondary batteries [11]. Spent LIB packs are fed into the kiln from the left side, as shown in Fig. 1, and they undergo pyro-processing in the cylindrical rotary kiln at 1 atm. The inside of the rotary kiln is usually adjusted to 800 °C by measuring with a thermocouple for temperature control. The solid objects obtained after pyro-processing in the rotary kiln are collected at the bottom of the exhaust chamber. Exhaust gases, where the temperature is approximately 770 °C, remain within the exhaust chamber after pyro-processing, and these gases enter the cyclone dust collector at the top side of the exhaust chamber. Fine powder particles are then collected in the cyclone dust collector. After the residual exhaust gas is burnt in the secondary combustion chamber, it is passed through a gas cooler and a bag filter to make it harmless and thereafter discharged from the chimney.

Fig. 2 shows the changes in the refractory thickness inside the kiln before and after conducting pyro-processing. The left side of this figure shows the refractory thickness prior to pyro-processing, whereas the right side shows the refractory thickness after pyro-processing 188 tons of small-scale LIB packs with an $LiCoO_2$ positive electrode, graphite negative electrode, and $LiPF_6$ electrolyte. This pyro-process was continuously carried out for

537 h. By comparing the refractory before and after LIB pyro-processing, the latter was observed to have peeled over the entire surface, and the thickness was reduced to approximately 125 mm. Because of the long continuous operation for 537 h, the time dependence of the change in refractory thickness could not be measured during the process, but an average erosion rate was estimated to be 0.13 mm per 1 ton of small-scale LIB packs. Usually, the refractory surface, which became black after pyro-processing the LIB, as shown in the right picture in Fig. 2, is cleaned and repaired during maintenance of the rotary kiln.

In this study, some parts of the refractory lining were sampled during the maintenance period of the rotary kiln and studied using various analysis techniques. As an example, two refractory specimens are shown in Fig. 3. The color of the inner LIB exposed surface was black, and at a depth of approximately 2–5 mm, the color was blue. These color changes of the refractory material correspond to the formation of various reaction layers.

2.2. SEM observation and EDX analysis

The fracture surface of the refractory specimens was subjected to coating with a layer of deposited carbon, and thereafter, the particle shape at the fracture surface was observed using field-emission scanning electron microscopy (FE-SEM; JSM-7001F from JEOL Ltd.). Furthermore, energy-dispersive X-ray analysis (EDX) was conducted to determine the composition of this observed part.

After a part of the refractory specimen was embedded with cured epoxy resin, it was mechanically sheared for cross-section analysis and then polished to a mirror finish. The polished surface was subsequently subjected to carbon coating, and then elemental mapping using the FE-SEM-EDX device (JXA-8230 from JEOL Ltd.) was conducted. The mapped elements included the refractory constituents of Al, Si, and Ca and the LIB constituents of F, P, and Co.

2.3. LIBS analysis

In this study, laser-induced breakdown spectroscopy (LIBS) was used for Li analysis because Li cannot be quantitatively measured using EDX. LIBS is used for non-contact measurements of the material composition, and it is applied for measuring various constituents, such as metal atoms in exhaust gas, ingredients in cement materials, and the alkaline components in air [14]. In LIBS, the laser beam is focused on the measurement area to form a plasma. Then, the material in the plasma is atomized and excited, and light of each atom-specific wavelength is radiated. By analyzing the light radiated by the plasma, it is possible to quantify the concentration of the constituents of the
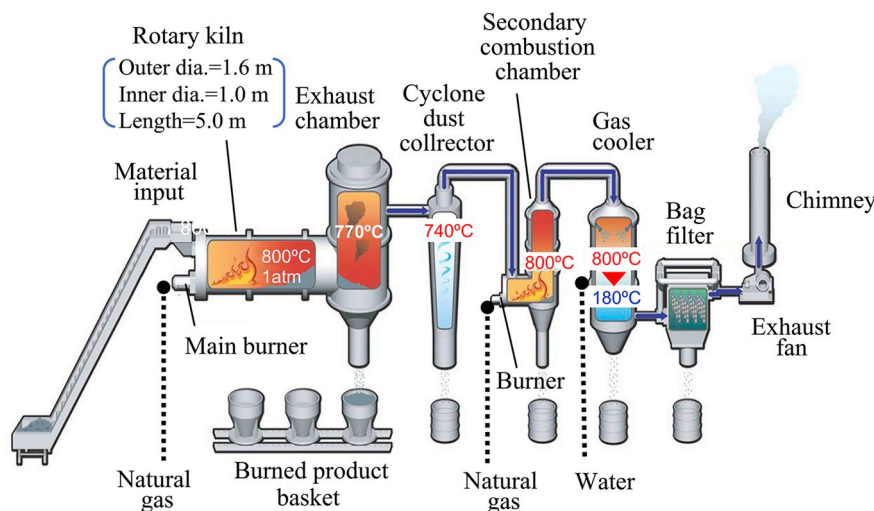

Fig. 1. Schematic diagram of rotary kiln used pyro-processing of used LIB packs [11].
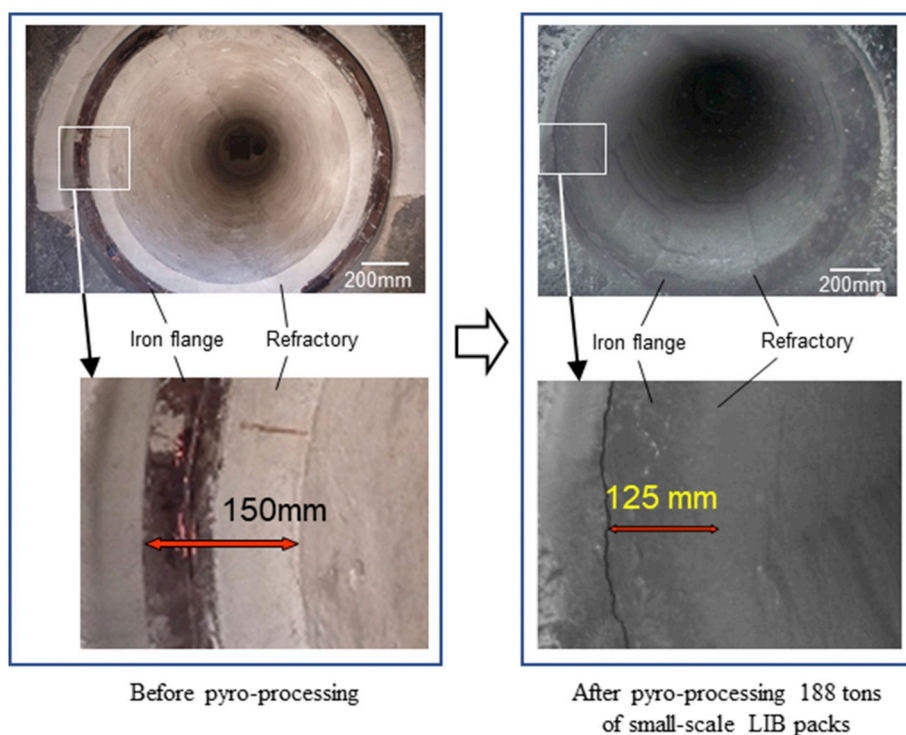
Fig. 2. The changes in refractory thickness inside the kiln before and after conducting pyro-processing.
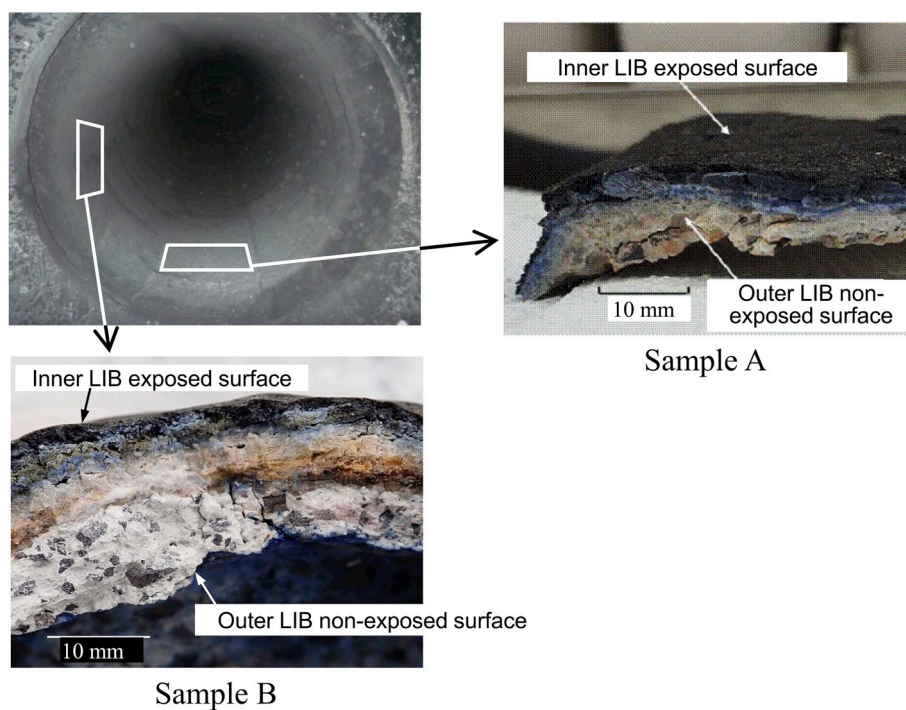

Fig. 3. Sampled refractory specimens.

material [15]. LIBS measurements were recorded at longitudinal intervals of 0.2 mm and at lateral intervals of 0.2 mm to estimate the Li concentration distribution on the measurement surface. The standard deviation of the Li concentration for each point was determined to be an average of 9.2% from five LIBS analyses.

2.4. Chemical analysis

Test specimens were sampled at depths of 0–2, 2–5, and 5–7 mm from the refractory lining, as shown in Fig. 3, ground to a powder, and subjected to acid dissolution and alkali fusion. The resulting solution was used in the quantitative analysis of Al, Si, Ca, Li, and P based on inductively coupled plasma atomic emission spectroscopy (ICP-AES). The standard deviations of each analyzed value were estimated to be less than 2.7% of the average value. Moreover, after alkali fusion with the mixture of sodium carbonate and sodium peroxide, the specimen was soaked in warm distilled water, and the concentration of F ions in the solution was quantitatively measured using ion chromatography.

The standard deviations of the analyzed F concentration were 4.1% of the average value.

2.5. Temperature measurement inside the rotary kiln

As mentioned above, the inside of the rotary kiln was controlled to 800 °C. However, to elucidate the refractory erosion mechanism, it was necessary to measure the combustion temperature of the LIB packs. For that purpose, a thermographic camera (measuring wavelength: 3.7–3.9 μm, Infrec R300BP-TF from Nippon Avionics Co. Ltd.) was used to measure the temperature inside the rotary kiln during LIB pyro-processing. The temperature measurement was carried out through a sapphire glass (2-mm thickness) on the rear hatch of the rotary kiln. The measured temperature was automatically corrected using the pre-measured emissivity of 0.97.

3. Results

3.1. SEM observations and EDX analyses of the damaged refractory materials

The SEM images of the unused refractory fracture surface are shown in Fig. 4. Mullite ($3Al_2O_3 \cdot 2SiO_2$) particles that were several micrometers in size were present as well as with Al_2O_3 clumps. The average concentrations of each element analyzed at five points on the mullite phase of the refractory material are provided to Fig. 4 and Table 1.

Fig. 5 shows the SEM images of the vertical cross section at a depth of 1–10 mm from the surface of the analyzed refractory specimen A shown in Fig. 3. The EDX analysis was repeated five times for various points of the same depth. Table 1 provides the average concentrations of each element on the refractory cross section as measured by EDX at the same locations as shown in the SEM images in Fig. 5. In this table, the same measurement results for sample B shown in Fig. 3 are also provided.

The particle shapes at the 1 mm depth in Fig. 5(a) were different from those of the unused refractory material shown in Fig. 4, and spherical particles were present that were several micrometers in size, and in the matrix, F and P, which were not detected in the unused refractory, were observed. In particular, the F concentration was found to be extremely high at 27 mass%, whereas the concentrations of the refractory constituents of Al, Si and Ca decreased. Additionally, amorphous flake-like particles were observed. The F and Al concentrations in the particles shown in Fig. 6(a) were 47 and 21 mass%, respectively. Therefore, those particles were likely composed of AlF_3.

The particles at the 2 mm depth were much coarser than the ones at the 1 mm depth, as shown in Fig. 5(b). The concentrations of Al, Si, and Ca in this area had reduced compared with those of the unused refractory material shown in Table 1, and the extent of reduction was smaller compared with that at the 1 mm depth.

As shown in Fig. 5(c), the particles at the 4 mm depth were even coarser and exhibited a shape different from that of the particles in the unused refractory shown in Fig. 4. These particles appeared to have solidified after melting. Upon comparing the constituent concentrations with those at the 2 mm depth, F decreased, but P increased to a

Fig. 4. SEM image and chemical composition (EDX-analysis) of the unused refractory cross-section.

concentration of 3.4%. Moreover, rod-shaped particles with sizes up to 20 μm were also observed in Fig. 5(c). The results of point analysis of the rod-shaped particles revealed a high concentration of P at 26 mass %, as shown in the table of Fig. 6(b).

Although the particles near the 5 mm depth shown in Fig. 5(d) were slightly larger than those of the unused refractory material shown in Fig. 4, the coarse particles observed at the 4 mm depth were not observed. The Al concentration of near the 5 mm depth shown in Table 1 was a little lower compared with that in the unused refractory, and the P and F concentrations were only 0.3 mass%.

Near the depth of approximately 7 mm, particles with several micrometers were observed, as shown in Fig. 5(e). The shapes of the particles were similar to those of the particles observed at the 5 mm depth, and they were slightly larger than the unused refractory particles shown in Fig. 4. Regarding the component concentrations, P had a 0.4 mass%, and F had a 0.2 mass%.

At a depth of approximately 10 mm, clumps of particles that were several micrometers were observed in Fig. 5(f), and they were a similar shape to the particles in the unused refractory material shown in Fig. 4. Moreover, the EDX results shows the constituent concentrations were almost the same as those of the unused refractory material, suggesting that there was no damage to the refractory material at this depth.

3.2. Elementary mapping using SEM-EDX

Fig. 7 shows the elementary mapping analysis results from SEM-EDX for the refractory cross section up to a depth of 5 mm from the surface. The concentrations of Al, Si and Ca were reduced up to a depth of approximately 2 mm. In particular, the reductions in the Si and Ca concentrations were significant. Phosphorus and F, which are electrolyte constituents of LIBs, penetrated up to a depth of approximately 5 mm. Fluorine was observed to be present in high concentration up to a depth of approximately 2 mm, and P was observed to be relatively uniformly dispersed up to a depth of approximately 5 mm. In particular, some concentrated parts were observed between depths of 4 mm and 5 mm. Cobalt, an active constituent of LIBs, was observed to be present up to a depth of 0.2 mm from the surface, but beyond that depth, it was not detected.

3.3. Lithium determination using LIBS

The Li analysis results of the refractory surface using LIBS are shown in Fig. 8(a). Clearly, Li was present throughout the surface, and the Li concentration was as high at approximately 15–20 mass%. The Li concentrations on the longitudinal cross section of the refractory material are shown in Fig. 8(b). Lithium penetrated up to a depth of approximately 3 mm. Most of the area has a concentration of 5–10 mass%, but there were also areas with a high concentration of 15–20 mass%.

3.4. Chemical analysis

Fig. 9 shows the chemical analysis results of the refractory surface in the depth direction from ICP-AES and ion chromatography. Lithium, P and F, which were not present at depths of 5–7 mm or in the unused refractory, were observed up to a depth of approximately 5 mm from the surface, and Al, Si, and Ca were found to be lower in concentration compared with those in the unused refractory. In the specimens at depths of 2–5 mm, Li, P, and F were more prevalent than at the surface, and the Si and Ca concentrations reduced significantly.

3.5. Results of XRD analysis

Although the compositions of each depth of the refractory were clarified as described in Sections 3.1 to 3.4, to investigate the formation of the mineral phases, X-ray diffraction (XRD) analysis was performed on the samples described in Section 3.4. The results are shown in Table 2, where the order of the first peak height of each mineral phase
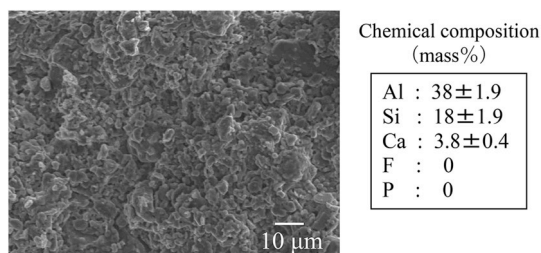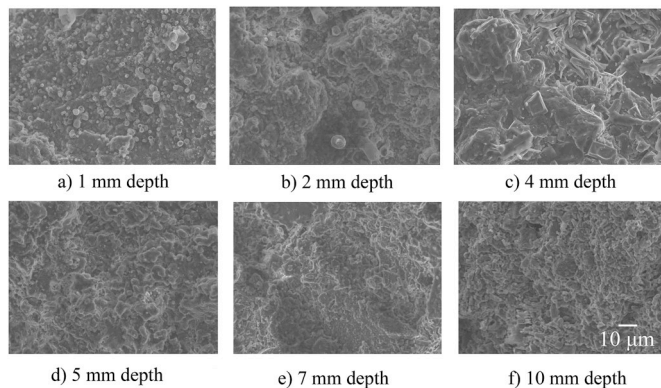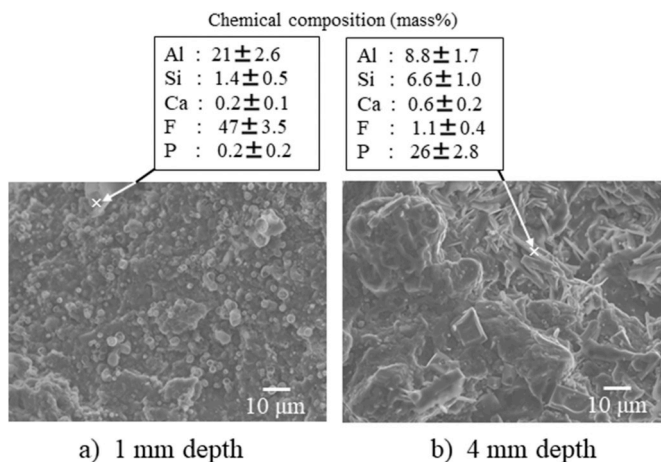
Table 1
Chemical composition on the refractory cross-section measured by EDX at the same parts of the SEM images shown in Figs. 4 and 5 (mass%).

Element	Unused	Analysis point					
		1 mm depth	2 mm depth	4 mm depth	5 mm depth	7 mm depth	10 mm depth
Sample A							
Al	38 ± 1.9	21 ± 2.2	24 ± 0.9	24 ± 3.3	31 ± 3.0	34 ± 2.0	39 ± 2.0
Si	18 ± 1.9	4.3 ± 0.9	12 ± 2.0	10 ± 2.9	23 ± 3.2	23 ± 2.1	18 ± 1.9
Ca	3.8 ± 0.4	0.0	1.4 ± 0.5	3.7 ± 0.7	5.8 ± 0.9	3.2 ± 0.6	4.0 ± 0.4
P	0.0	0.7 ± 0.2	0.7 ± 0.2	3.4 ± 0.8	0.3 ± 0.2	0.4 ± 0.2	0.2 ± 0.1
F	0.0	27 ± 2.6	18 ± 1.9	1.6 ± 0.7	0.3 ± 0.2	0.2 ± 0.1	0.1 ± 0.1
Sample B							
Al		26 ± 2.1	25 ± 0.9	25 ± 3.3	33 ± 4.1	35 ± 2.6	37 ± 2.5
Si		10 ± 0.9	15 ± 1.6	14 ± 1.9	20 ± 3.3	22 ± 1.9	20 ± 1.9
Ca		0.5 ± 0.1	1.5 ± 0.3	3.6 ± 0.7	3.6 ± 1.0	3.2 ± 0.3	3.0 ± 0.3
P		0.8 ± 0.3	0.9 ± 0.2	4.4 ± 1.2	0.3 ± 0.2	0.1 ± 0.1	0.1 ± 0.0
F		19 ± 1.6	13 ± 1.3	1.5 ± 0.5	0.3 ± 0.2	0.2 ± 0.1	0.1 ± 0.0

a) 1 mm depth b) 2 mm depth c) 4 mm depth

d) 5 mm depth e) 7 mm depth f) 10 mm depth

Fig. 5. SEM images of the cross-section at a depth of 1–10 mm from the surface of the analyzed refractory specimen (sample A in Fig. 3).

Chemical composition (mass%)

Al : 21±2.6	Al : 8.8±1.7
Si : 1.4±0.5	Si : 6.6±1.0
Ca : 0.2±0.1	Ca : 0.6±0.2
F : 47±3.5	F : 1.1±0.4
P : 0.2±0.2	P : 26±2.8

a) 1 mm depth b) 4 mm depth

Fig. 6. SEM images at 1 mm depth and compositions of amorphous flake-like particles (a) and that at 4 mm depth and chemical compositions of rod-shaped particles (b).

was L > M > s > ss. In the refractory before pyro-processing, Al_2O_3 (Corumdum) and Al_2SiO_5 (Sillimanite) were mainly present; however, after pyro-processing the LIB packs, $LiAlO_2$ and $LiAlSiO_4$ were identified at both 0–2 mm depths and 2–5 mm depths. The failure to identify mineral phases containing P_2O_5 was likely owing to the lack of the American Society for Testing and Materials (ASTM) data. Therefore, we concluded that establishment of an Li_2O–Al_2O_3–SiO_2–P_2O_5(-LiF) phase diagram is necessary to explain the new phase generation during LIB pyro-processing.

3.6. Temperature during pyro-processing

The thermographic camera measurement results of the temperature inside the rotary kiln during pyro-processing of the LIB packs are shown in Fig. 10. The maximum temperature measured was 1292 °C. There were variations in temperature inside the rotary kiln during the pyro-processing of the LIB packs, and a localized temperature increase to approximately 1300 °C was observed.

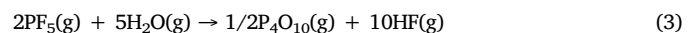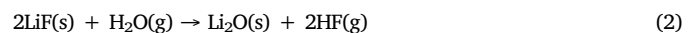## 4. Discussion on refractory damage

Based on the analyzed data of the damaged refractory, as mentioned above, the following factors were considered.

A reduction in the refractory constituents Al, Si and Ca up to a depth of approximately 2 mm from the surface may have occurred in the following manner.

First, owing to thermal decomposition of $LiPF_6$ in the LIB electrolyte, where the solvent was liquid propylene carbonate, elementary reaction (1) can occur above 127 °C [16]. Because the boiling point of propylene carbonate is 242 °C [17], $LiPF_6$ in the LIB electrolyte precipitates above 242 °C. The boiling point of PF_5 is −85 °C [18], and the melting and boiling points of LiF are 848 °C and 1673 °C [19], respectively. Therefore, reaction (1) will proceed in the temperature range of 242–848 °C.

$$LiPF_6(s) \rightarrow LiF(s) + PF_5(g) \tag{1}$$

When the generated LiF solid and PF_5 gas react with the steam, which is generated during the thermal decomposition of organic materials, such as the electrolyte solution (propylene carbonate), separator, and pack resin, HF will be produced according to Eqs. (2) and (3) at the operation temperature (800 °C), where the boiling points of Li_2O are 1200 °C [20] and 1330 °C [21], although its melting points are 1438 °C [19], 1727 °C [22], and 1430 °C [23], and where the melting and boiling points of P_2O_5 (P_4O_{10}) are 570 °C and 605 °C, respectively [19].

$$2LiF(s) + H_2O(g) \rightarrow Li_2O(s) + 2HF(g) \tag{2}$$

$$2PF_5(g) + 5H_2O(g) \rightarrow 1/2P_4O_{10}(g) + 10HF(g) \tag{3}$$

When combining reactions (1), (2), and (3), it is expressed as reaction (4) above 605 °C.

$$2LiPF_6(s) + 6H_2O(g) \rightarrow Li_2O(s) + 1/2P_4O_{10}(g) + 12HF(g) \tag{4}$$
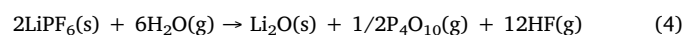
Along with the generation of Li_2O, P_4O_{10}, and HF, LiF formation is predicted by reaction (5) by combining reactions (1) and (3).

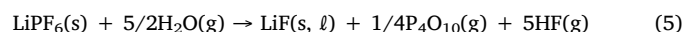$$LiPF_6(s) + 5/2H_2O(g) \rightarrow LiF(s, \ell) + 1/4P_4O_{10}(g) + 5HF(g) \tag{5}$$

Fig. 11 shows the standard Gibbs free energy of reactions (4) and (5) with respect to the temperature obtained by combining the respective
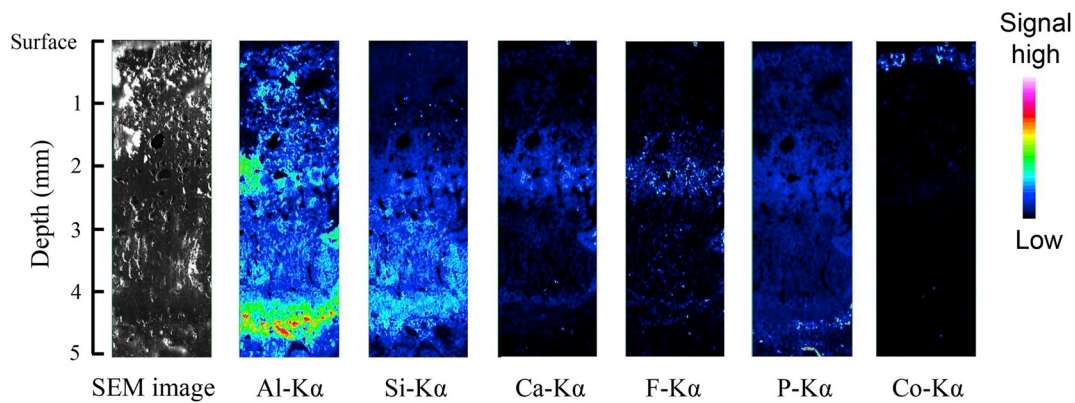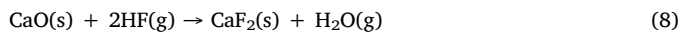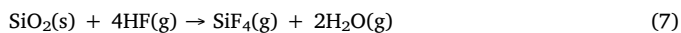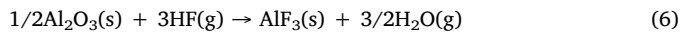
Fig. 7. SEM image and EDX elementary mappings for the refractory cross-section up to a depth of 5 mm.

thermodynamic data [24]. In this figure, M(*i*) and B(*i*) denote the melting and boiling points of *i*, respectively. Assuming that each reactant and product are in the standard state (pure substances), it can be seen from this figure that equation (4) proceeds to the right above 530 °C and equation (5) proceeds to the right above 220 °C. Additionally, above 782 °C, equation (4) will prevail over equation (5). Thus, at operating temperatures of 800 °C and 1300 °C, as described in Section 3.6, $Li_2O(s)$, $P_4O_{10}(g)$, and HF(g) are mainly generated.

The HF generated in reaction (4) may cause the erosion of Al_2O_3, SiO_2, and CaO in the refractory following reactions (6), (7) and (8), respectively, because the sublimation point of AlF_3 is 1276 °C [19] and the boiling point of SiF_4 is −86 °C [25], whereas the melting and boiling points of CaF_2 are 1418 °C and 2500 °C, respectively [19].

$$1/2Al_2O_3(s) + 3HF(g) \rightarrow AlF_3(s) + 3/2H_2O(g) \quad (6)$$

$$SiO_2(s) + 4HF(g) \rightarrow SiF_4(g) + 2H_2O(g) \quad (7)$$

$$CaO(s) + 2HF(g) \rightarrow CaF_2(s) + H_2O(g) \quad (8)$$

The temperature dependence of the standard free energies of reactions (6) to (8) obtained from thermodynamic data [24] are shown in Fig. 12, where $M(CaF_2)$ and $S(AlF_3)$ denote the melting points of CaF_2 and the sublimation point of AlF_3, respectively. Similar to the data

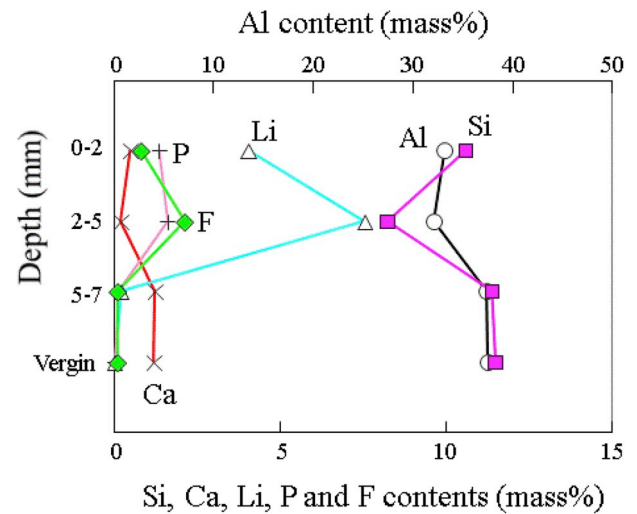**Fig. 9.** Results of chemical analysis of the refractory in the depth direction.

(a) Refractory surface
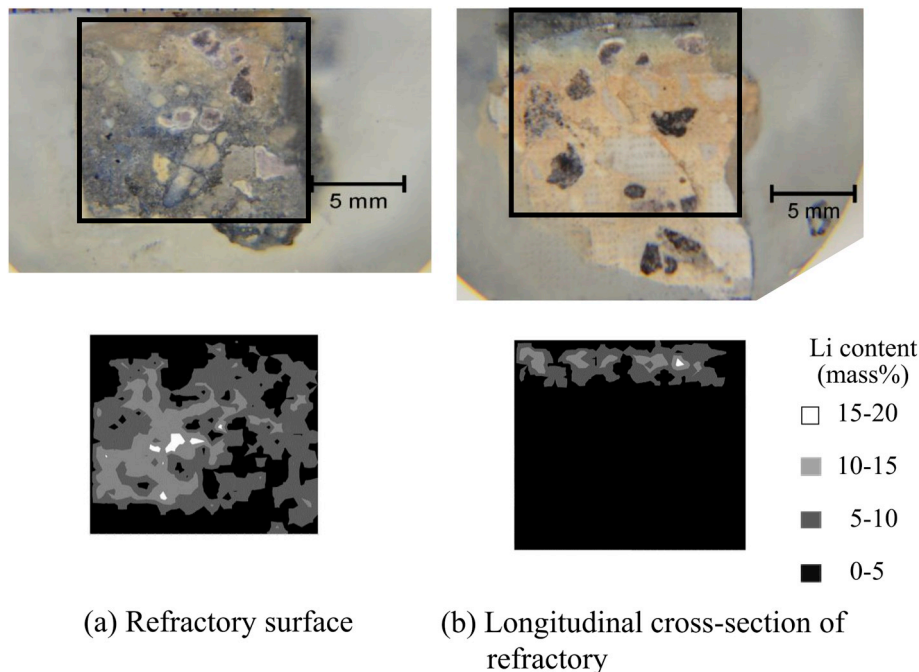
(b) Longitudinal cross-section of refractory

Fig. 8. Li concentration mappings on the refractory surface (a) and the longitudinal cross-section (b) of the refractory sample A obtained by LIBS.
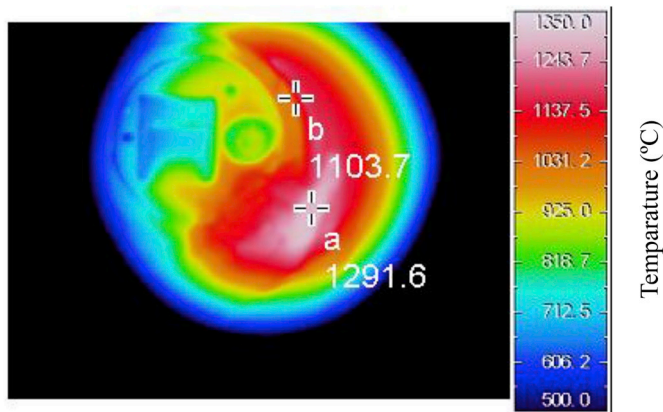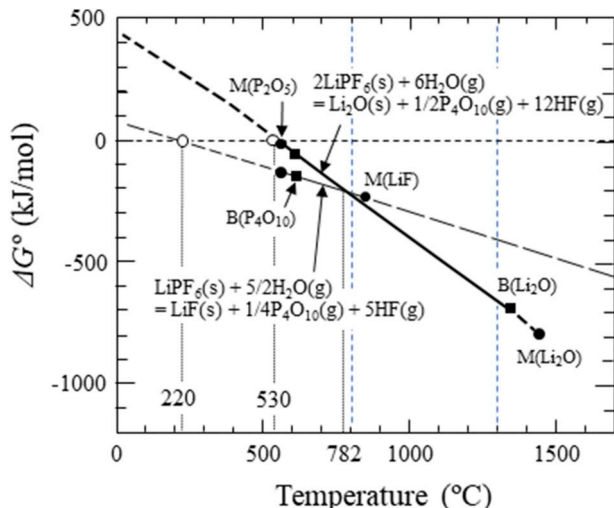
Table 2
Mineral phases in each part of the refractory identified by XRD.

Minera phase	Vergin	0–2 mm depth	2–5 mm depth	5–7 mm depth
Al_2O_3 Corundum	L			L
$Al_6Si_2O_{13}$ (Mullite)	s			s
Al_2SiO_5 (Sillimanite)	L			L
SiO_2	M			M
$LiAlO_2$		L	L	
$LiAl_5O_8$		s	s	
$LiAlSiO_4$		M	M	
LiF		ss	s	
$LiCoO_2$		s	ss	

Peak height: L > M > s > ss.

Fig. 10. Temperature inside the rotary kiln during pyro-processing of LIB packs.

Fig. 11. Standard Gibbs free energies of reactions (4) and (5) plotted against temperature.

shown in Fig. 11, assuming that each reactant and product are in the standard state (pure substances), equations (6) and (7) proceed to the right below 820 °C and 932 °C, respectively. Equations (8) can always occur in the temperature range indicated in Fig. 12. This means that during heating to an operating temperature of 800 °C, equations (6)–(8) could occur. Additionally, CaF_2 may vaporize upon the formation of an azeotropic compound with AlF_3 and/or SiF_4. Presumably, this refractory erosive reaction occurs because of a mechanism similar to that observed during the damage to the refractory by fluorine gas in waste incinerators, as reported by Yamamoto [26]. This damage mechanism is schematically shown for the refractory surface part shown in Fig. 13(a).
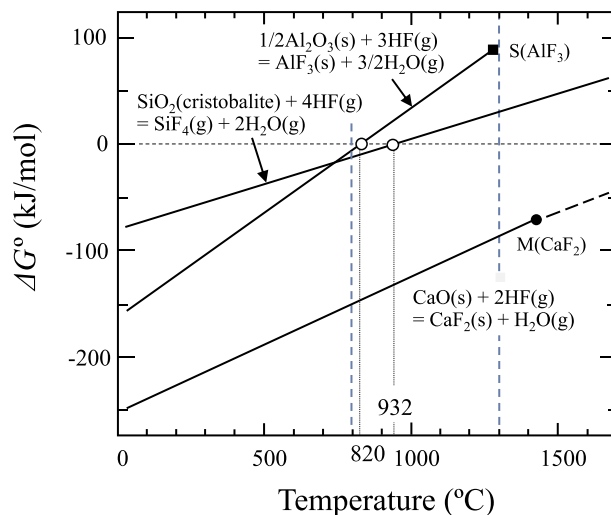
Fig. 12. Standard Gibbs free energies of reactions (6) to (8) plotted against temperature.

As shown in Figs. 5(c) and 6(b), at a depth of approximately 4 mm from the surface of the refractory, the particles generated appeared to have melted and solidified, and a high concentration of P was detected at this depth. Moreover, Li was observed to have penetrated to a depth of approximately 3 mm, as shown in Fig. 8(b), and up to a depth of approximately 5 mm, as shown in Fig. 9. The temperature inside the kiln increased to approximately 1300 °C, as shown in Fig. 10. Consequently, as a second mechanism of refractory damage, erosion occurred because the refractory melting point was lowered by Li_2O, P_2O_5 and fluorides that formed via reactions (4) to (8). Thus, at high temperature, an $Li_2O–Al_2O_3–SiO_2–P_2O_5$(-LiF) melt can generate (Fig. 13(a)), and this low-melting-point melt penetrates easily into the refractory through pores, grain boundaries, and cracks (Fig. 13(b)), causing a peeling phenomenon (Fig. 13(c)). To confirm this hypothesis, the phase diagrams of the $Li_2O–Al_2O_3–SiO_2–P_2O_5$(-LiF) system should be studied. From another point of view, it is expected to be preferable to use an MgO refractory with a gradient composition, which has been recently indicated to be resistant to the erosion of the $Al_2O_3–SiO_2–CaO–CaF_2$ melt by Han et al. [27].

5. Conclusion

During pyro-processing of an LIB in a rotary kiln to recycle the spent LIB, a phenomenon occurs in which the thickness of the refractory lining inside the kiln becomes reduced. In this study, to elucidate the factors of refractory damage, a composition analysis of the damaged refractory was conducted using FE-SEM-EDX, LIBS, ICP-AES, XRD, and ion chromatography, and the following three conclusions were made.

(1) In the refractory material up to approximately a 5-mm depth from the surface, the Al, Si, and Ca concentrations were observed to be lower than those in the unused refractory. In particular, at a depth of approximately 2–5 mm, Li, P, and F were observed to have higher concentrations than at the refractory surface, whereas the Si and Ca concentrations decreased significantly.

(2) From the results of localized analysis, the Al, Si, and Ca concentrations decreased up to approximately a 2-mm depth from the surface. Phosphorus and F were observed to have penetrated up to a 5-mm depth. A high concentration of F was observed at a depth of 2 mm. Phosphorus was observed to be relatively uniformly concentrated up to a depth of 5 mm, and in particular, there were areas of high concentration near depths of 4–5 mm. In contrast, Li was observed to be in high concentration up to a depth of 3 mm.

(3) Up to a depth of approximately 4 mm from the surface, the refractory particle shape was observed to have changed compared
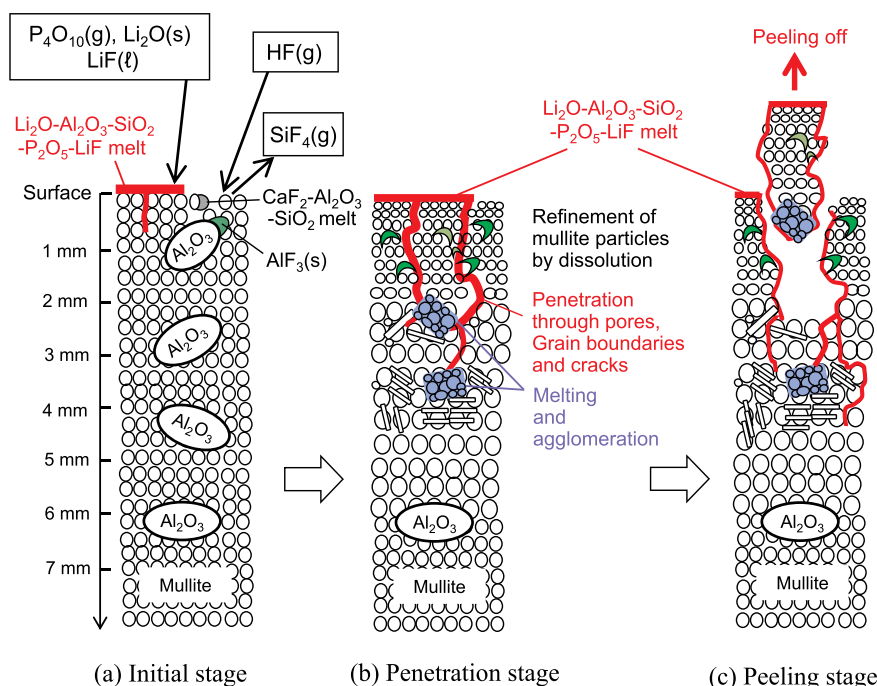
Fig. 13. Schematic illustration of refractory damage mechanism.

with that of the unused refractory. At a 1-mm depth, particles that were several micrometers in size were observed, and at depths of 2–4 mm, course particles that appeared to have melted and solidified were observed.

Based on the aforementioned observations, the following two mechanisms of refractory damage were derived.

(4) The constituents of an LIB electrolyte decompose at a high combustion temperature and react with steam to produce Li_2O, P_2O_5, HF, and LiF. This HF subsequently undergoes a gas–solid reaction with the refractory constituents of Al_2O_3, SiO_2 and CaO, resulting in the depletion of the refractory constituents.

(5) At high temperatures, from the reaction of Li_2O and P_2O_5 (as well as LiF) with the refractory constituents of Al_2O_3 and SiO_2, a low-melting-point phase forms and penetrates into the refractory through pores, grain boundaries and cracks, resulting in peeling off.

Appendix A. Supplementary data

Supplementary data to this article can be found online at https://doi.org/10.1016/j.ceramint.2019.12.182.

References

[1] Fuji Keizai Co Ltd, Overall Status Survey of Battery Related Market vol. 1, (2016).
[2] M. Idrees, S. Batool, Q. Zhuang, J. Kong, I. Seok, J. Zhang, H. Liu, V. Murugadoss, Q. Gao, Z. Guo, Achieving carbon-rich silicon-containing ceramic anode for advanced lithium ion battery, Ceram. Int. 45 (2019) 10572–10580.
[3] Y.M. Yang, C. Loka, D.P. Kim, S.Y. Joo, S.W. Moon, Y.S. Choi, J.H. Park, K.-S. Lee, Si-FeSi$_2$/C nanocomposite anode materials produced by two-stage high-energy mechanical milling, Met. Mater. Int. 23 (2017) 610–617.
[4] J. Xu, H.R. Thomas, R.W. Francis, K.R. Lum, J. Wang, B. Liang, A review of processes and technologies for the recycling of lithium-ion secondary batteries, J. Power Sources 177 (2008) 512–527.
[5] T. Georgi-Maschler, B. Friedrich, R. Weyhe, H. Heegn, M. Rutz, Development of a recycling process for Li-ion batteries, J. Power Sources 207 (2012) 173–182.
[6] S. Koyanaka, K. Horai, H. Kawai, S. Kato, J. Shibata, N. Murayama, T. Ohki, M. Masuda, A study on selective crushing and physical separation of roasted spent lithium ion batteries, J. MMIJ 128 (2012) 232–240.
[7] K. Horai, J. Shibata, N. Murayama, S. Koyanaka, M. Niinae, Recycling technology

for lithium ion battery by crushing and classification, and hydrometallurgical process, J. Jpn. Inst. Met. Mater. 78 (2014) 250–257.
[8] V.T. Nguyen, J.-C. Lee, J. Jeong, B.-S. Kim, B.D. Pandey, Selective recovery of cobalt, nickel and lithium from sulfate leachate of cathode scrap of Li-ion batteries using liquid-liquid extraction, Met. Mater. Int. 20 (2014) 357–365.
[9] L. Yang, G. Xi, Y. Xi, Recovery of Co, Mn, Ni, and Li from spent lithium ion batteries for the preparation of LiNi$_x$Co$_y$Mn$_z$O$_2$ cathode materials, Ceram. Int. 41 (2015) 11498–11503.
[10] N. Tamura, T. Hanada, Y. Ishida, T. Honda, H. Kamiya, K. Sakai, The study of technology for recycling the automotive lithium-ion battery, Proceedings of the 27th Annual Conference of Japan Society of Material Cycles and Waste Management, 2016, pp. 167–168.
[11] Nippon Recycle Center Corporation HP, http://www.recycle21.co.jp/index.html.
[12] Y. Murakami, Y. Matsuzaki, K. Murakami, S. Hiratani, A. Shibayama, R. Inoue, Recovery rates of used rechargeable lithium-ion battery constituent elements in heat treatment, submitted to, Metall. Mater. Trans. B 33 (2020).
[13] X. Duan, H. Zheng, Y. Chen, F. Qian, G. Liu, X. Wang, Y. Si, Study on the corrosion resistance of cordierite-mullite and SiC refractories to Li-ion ternary cathode materials, Ceram. Int. 45 (2019).
[14] M. Noda, Y. Deguchi, S. Dobashi, K. Yoshikawa, S. Iwasaki, Trace element detection using laser diagnostics, Rev. Laser Eng. 29 (2001) 164–168.
[15] H. Kondo, M. Aimoto, K. Wagatsuma, Optical emission spectrometry for optimization of steelmaking processes, Tetsu-To-Hagané 100 (2014) 846–856.
[16] K.S. Gavrichev, G.A. Sharpataya, L.N. Golushina, V.N. Plakhotnik, I.V. Goncharova, Heat capacity and thermodynamic functions of LiPF$_6$, Russ. J. Inorg. Chem. 47 (2002) 940–944.
[17] N. Rajapakse, H.L. Finston, V. Fried, J. Chem. Eng. Data 31 (1986) 408–410.
[18] S. Budavari (Ed.), The Merck Index - Encyclopedia of Chemicals, Drugs and Biologicals, Merck and Co., Inc., Rahway, NJ, 1989, p. 1168.
[19] The engineering ToolBox, https://www.engeeringtoolbox.com/inorganic-salt-melting-boiling-point-water-solubility-density-liquid-d_1984.html.
[20] READE, Your speciality chemicals resource, https://www.reade.com/products/lithium-oxide-powder-li2o.
[21] J. Beck, ResearchGate https://www.researchgate.net/post/Reaction_between_Lithium_Oxide_Li2O_and_Silicon_Si.
[22] S.S. Kim, T.H. Sanders Jr., Thermodynamic modeling of phase diagrams in binary alkali silicate systems, J. Am. Ceram. Soc. 74 (1991) 1833–1840.
[23] S. Claus, H. Kleykamp, W. Smykatz-Kloss, Phase equilibria in the Li4SiO4-Li2SiO3 region of the pseudobinary Li2O-SiO2 system, J. Nucl. Mater. 230 (1996) 8–11.
[24] M.W. Chase Jr., NIST-JANAF thermochemical tables, Monograph, J. Phys. Chem. Ref. Data 9 (1998) 99, 154, 716, 729, 1055, 1190, 1323, 1751, fourth ed..
[25] R.L. Brown, S.E. Stein, NIST chemistry WebBook, SRD 69, https://webbook.nist.gov/cgi/cbook.cgi?ID=C7783611&Units=SI&Mask=4.
[26] T. Yamamoto, Damage to refractory by fluorine gas in waste incinerator, Ceramics (Japan) 45 (2010) 30–34.
[27] J.S. Han, J. Chung, J.H. Park, Influence of exposure temperature on degradation of magnesia refractory by steel refining slags, Met. Mater. Int. 25 (2019) 1360–1365.